Geoscience Frontiers 13 (2022) 101405

Contents lists available at ScienceDirect

Geoscience Frontiers

journal homepage: www.elsevier.com/locate/gsf

Research Paper

Nanoscale mechanical property variations concerning mineral composition and contact of marine shale

Yong Li [a,*], Jianqi Chen [a], Derek Elsworth [b], Zhejun Pan [c], Xiaotian Ma [a]

[a] State Key Laboratory of Coal Resources and Safe Mining, College of Geosciences and Surveying Engineering, China University of Mining and Technology, Beijing 100083, China
[b] Department of Energy and Mineral Engineering, Geosciences, EMS Energy Institute and the G3 Center, Pennsylvania State University, University Park, PA 16802, USA
[c] Key Laboratory of Continental Shale Hydrocarbon Accumulation and Efficient Development, Ministry of Education, Northeast Petroleum University, Daqing, Heilongjiang 163318, China

ARTICLE INFO

Article history:
Received 2 January 2022
Revised 20 April 2022
Accepted 12 May 2022
Available online 19 May 2022
Handling Editor: W.G. Zhang

Keywords:
Shale oil and gas
Shale lithofacies
Mineral composition
Multiscale mechanical property
Nanoscale mechanics
Finite-element simulation

ABSTRACT

Mechanical properties of shales are key parameters influencing hydrocarbon production – impacting borehole stability, hydraulic fracture extension and microscale variations in *in situ* stress. We use Ordovician shale (Sichuan Basin, China) as a type-example to characterize variations in mineral particle properties at microscale including particle morphology, form of contact and spatial distribution *via* mineral liberation analysis (MLA) and scanning electron microscopy (SEM). Deformation-based constitutive models are then built using finite element methods to define the impact of various architectures of fracture and mineral distributions at nanometer scale on the deformation characteristics at macroscale. Relative compositions of siliceous, calcareous and clay mineral particles are shown to be the key factors influencing brittleness. Shales with similar mineral composition show a spectrum of equivalent medium mechanical properties due to differing particle morphology and mineral heterogeneity. The predominance of small particles and/or point-point contacts are conducive to brittle failure, in general, and especially so when quartz-rich. Fracture morphology, length and extent of filling all influence shale deformability. High aspect-ratio fractures concentrate stress at fracture tips and are conducive to extension, as when part-filled by carbonate minerals. As fracture spacing increases, stress transfer between adjacent fractures weakens, stress concentrations are amplified and fracture extension is favored. The higher the fractal dimension of the fracture and heterogeneity of the host the more pervasive the fractures. Moreover, when fractures extend, their potential for intersection and interconnection contributes to a reduction in strength and the promotion of brittle failure. Thus, these results provide important theoretical insights into the role of heterogeneity on the deformability and strength of shale reservoirs with practical implications for their stimulation and in the recovery of hydrocarbons from them.

1. Introduction

Shale comprises a heterogeneous and typically laminated fine-grained assemblage of minerals imparting both strong anisotropy and low permeability (Ma et al., 2016; Ougier-Simonin et al., 2016; Anastasia et al., 2017; Li et al., 2019; Zou et al., 2019). Such strong heterogeneity and anisotropy in mechanical and transport properties exert strong control on the recovery of hydrocarbon fluids. In particular, the mechanical response exerts key control on the successful recovery of oil and gas through wellbore stability, hydraulic fracturing and in situ stresses and their spatial variation (Davis and Moin, 2016; Gholami et al., 2018; Labani and Rezaee, 2015; Meier et al., 2015; Shrey and Brijes, 2015; Zhang et al., 2019). Mechanical properties are typically evaluated at macroscale using standard core-based experiments to measure equivalent-medium deformability and strength (Sone and Zoback, 2013; Liang et al., 2021). The effects of lamination/bedding on the orientation-dependent brittleness of shales may be related to fractal characteristics and independently measured (Zhang et al., 2018; Chen et al., 2021; Fan et al., 2021a, 2021b). Similarly, the effects of anisotropy on hydraulic fracturing may be characterized using X-ray CT (Arif et al., 2020; Guo et al., 2021) with acoustic emission defining impacts of damage on the resulting fracture (Moradian et al., 2016; Ban et al., 2020). However, despite such routine mechanical tests at macroscale, these observations defy deconvolution from grain-scale measurements that may require micro- or even nanometer scale resolution. Moreover, recovering undisturbed samples

* Corresponding author.
E-mail address: liyong@cumtb.edu.cn (Y. Li).

https://doi.org/10.1016/j.gsf.2022.101405

of sufficient dimension from depth is difficult – making the reconstruction of mechanical and transport properties from small samples of recovered drilling cuttings particularly attractive.

Thus, micro-scale petrophysical techniques can partially remedy such limitations in sampling and allowing the direct determination in anisotropy, deformability and brittleness of target reservoirs by combining seismic imaging with logging information (Huo et al., 2018a, 2018b; Wang et al., 2018). Dipole array acoustic logging effectively evaluates mechanical parameter profiles, yielding estimates of elastic modulus and Poisson ratio (Wetherington and Steer, 2012) – but sometimes with significant uncertainties. The anisotropy of shale mechanical properties is the result of the combination of organic and clay mineral orientation, brittle mineral composition, pore-fracture development, and other factors (Weijermars et al., 2020; Wild and Amman, 2018). Thus, in constructing physical models, isotropic self-consistent models (SCA), differential equivalent medium models (DEM), V-R-H (Voigh-Reuss-Hill) boundaries and H-S (Hashin-Shtrikman) bounds are all adopted (Hu et al., 1949; Bandyopadhyay, 2009). Inclusion of observations of clay mineral orientation, lamination distribution, pore and fracture structure, organic matter maturity and fluid hydrocarbon characteristics all improve the representativeness and accuracy of the physical model (Deng et al., 2019; Falahat and Farrokhnia, 2020).

Such models require measurement of pointwise properties at micro- to nano-scale with both nanoindentation and atomic force microscopy (AFM) (Simon et al., 2016; Shi et al., 2019; Milliken and Hayman, 2019; Li et al., 2020) providing essential data. Thus, triaxial compression data at large-scale, together with nanoindentation and AFM at small-scale may be effectively scaled and coupled to yield useful descriptors of equivalent-medium response (Li et al., 2020, 2021). Geomaterials are formed by fine particles and other media through hundreds of millions of years of physical and chemical processes (Zhang et al., 2018; Shahin et al., 2019; Liu et al., 2022). The architecture of mineral composition and distribution and the presence and morphology of fractures at micro-scale all impact response in such stress-sensitive materials – the relative impacts uncertain and remaining to be defined.

To address this uncertainty, we apply mineral liberation analysis (MLA) to define the mineral distribution in Ordovician shales from the Longmaxi Formation, Sichuan Basin, China. We apply scanning electron microscopy (SEM) to characterize the form of the contacts between adjacent minerals and the morphology of microfractures, both at nano-meter scale. Shale aggregates with systematically defined architectures are then reconstructed as finite element models to honor various mineral distributions and topologies, particle sizes and contact relationships and loaded to define microscopic stresses and deformations and macroscopic equivalent medium properties. Observations from these virtual experiments are then used to improve our insights into the key mechanisms and controls on the mechanical and geophysical response of shales across the scales.

2. Methodology

We select a series of four core samples and characterize the composition, size and distribution of component minerals. These compositional distributions are then represented by fractal analysis and replicated in distributed-parameter finite element models to define macroscopic deformation parameters.

2.1. Samples and experiment

The four shales were sampled from the Ordovician – Silurian Longmaxi Formation, Jiaoshiba area, Sichuan Basin, China (Fig. 1a). The Jiaoshiba area is located in the southeastern of the Sichuan Basin, and the sampled shale was deposited in a deep shelf facies (Zhang et al., 2017). The shale is mainly of Type I to II_1 kerogen, with total organic carbon content > 2.0 %, and vitrinite reflectance R_o around 2.0% to 3.5% (Wang et al., 2019). The shales with commercial gas production are generally of relatively high porosity > 5% and high gas content > 3.0 m^3/t (Zou et al., 2016).

Among the four recovered fresh sample fragments, relatively regular specimens were selected for argon ion polishing (Fig. 1c) to observe the micro mineral distribution and contact. The rest debris were tested by *X*-ray diffraction (XRD) to acquire the mineral composition. Samples to be tested by MLA were first argon-ion polished by a three-ion beam on a Leica EM TIC 3X. The argon-ion beam denudes the sample layer-by-layer to polish the surface. The ion beam acceleration voltage was 6 kV with a gun current of 2.2 mA and a duration of polishing of 4 h.

The MLA comprises an SEM and X-ray spectrometer together with appropriate processing software. The software supports the automated measurement and subsequent image processing, mineral editing and data output. The MLA instrument is an FEI MLA250 located at the Chinese Academy of Sciences (Institute of Geology and Geophysics, Beijing). This apparatus includes automatic mineral analysis and testing with an energy dispersive X-ray fluorescence spectrometer for automatic scanning and energy spectrum analysis. The SEM images of the sample were obtained at an acceleration voltage of 25 kV and beam current of 10 nA. Different mineral phases were distinguished pixel-by-pixel by considering the difference in the grayscale values allowing automated and synchronous mineral raster identification.

The mineral raster measured voxel-by-voxel by MLA represents a microscopic profile of shale architecture not representative of the macroscale bulk composition of the sample. Thus, XRD equipment D/max-pc2500x was used to determine the averaged whole-rock mineral composition. A fresh sample of ~ 50 g was first crushed and segregated to < 80 mesh with 10 g of this further ground in an agate mortar to < 300 mesh. Copper X-ray tubes operating at 40 kV and 30 mA were then used with counts collected from 3° to 90° in steps of 0.02° and at a speed of 3°/min - to obtain an accurate mineral composition of the aggregate sample.

2.2. Key parameters acquired from image analysis

We use the images recovered by MLA and SEM to define the mineral heterogeneity of, and the fracture distributions in, the sample and apply fractal concepts to codify these.

2.2.1. Fractal dimension of mineral distribution

The box dimension method is adopted to calculate the fractal dimension of the individual minerals comprising the sample. The method superimposes a grid of small boxes of side-length ε over the sample image (graph) and then calculates the number of boxes $N(\varepsilon)$ filled by that specific mineral. By reducing the size of the boxes, ε, the resulting $N(\varepsilon)$ naturally increases. The slope of the linear portion of the curve representing the number of filled cells ($N(\varepsilon)$) *-versus-* cell edge dimension (ε) in log–log space defines the fractal dimension D as,

$$D = -\lim_{\varepsilon \to 0} \frac{\ln N(\varepsilon)}{\ln \varepsilon} \quad (1)$$

as a power spectral density. The image processing in this study uses digital images of the mineral distribution with segmenting software (Photoshop) to extract maps of individual mineral boundaries and to recover the real combination characteristics and contact relations of the minerals. These images are then binarized in MATLAB to calculate fractal dimension for each mineral.

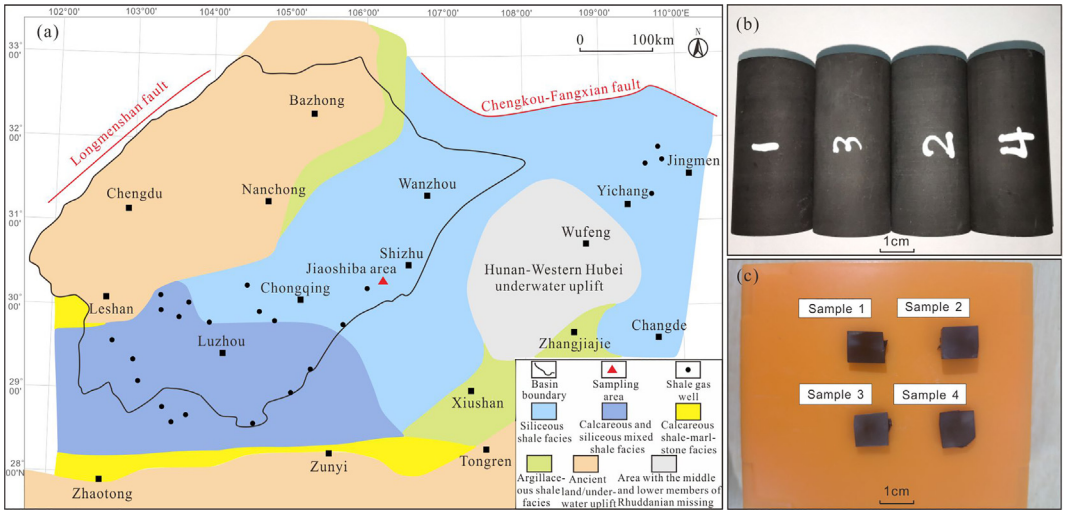

Fig. 1. Samples location and their exterior characteristic. (a) Location map of Sichuan Basin (Wang et al., 2019). (b) Column samples showing the shale exterior, about 25 mm diameter and 50 mm length. (c) Samples polished by argon ion, with sizes about 10 mm length, 10 mm width and 5 mm thickness.

2.2.2. Mineral heterogeneity coefficient

The variation coefficient d_i of minerals along a certain directional azimuth is calculated as (Wu et al., 2020),

$$d_i = \frac{\sigma_i}{\mu_i} \tag{2}$$

where, σ_i is the standard deviation of the content of a mineral in the i^{th} direction, μ_i is the mean value of the line content of a mineral in that direction i. The line $C_{(s)}$ content of a mineral on any measured trajectory is calculated as,

$$C_{(s)} = \frac{\int f(x)dx}{L} \tag{3}$$

where, f(x) is the content of the mineral at position × and L is the total length of the measurement scanline. Mean and standard deviation are then calculated as,

$$\mu_i = \sum \frac{C(s)}{n} \tag{4}$$

and

$$\sigma_i = \sqrt{\frac{\sum (C(s) - \mu_i)^2}{n}} \tag{5}$$

where, n is the number of lines of the mineral in the specific s direction. Referring to the definition of macroscopic anisotropy, the coefficient of variation in any two orthogonal directions is used to establish the parameter describing microscopic heterogeneity. Thus, the mineral microscopic heterogeneity coefficient is calculated as,

$$A_n = (d_i - d_i')/2d_i' \tag{6}$$

where, d_i is the coefficient of variation in some azimuth and d_i' is the orthogonal coefficient of variation in the principal azimuth.

2.2.3. Fracture development degree

A fractal dimension may be applied to define the distribution and cross-sectional complexity of fractures – anticipated to directly influence the mechanical properties and fluid-transmission characteristics. Fracture morphology is typically complex and micro/nano-scale heterogeneity typically high. Thus, the complexity of the fracture network is defined by the heterogeneity between matrix and fracture system – allowing similar fractal characterizations to be applied as noted before. The fractal dimension accommodating fracture trace length may be calculated (Eq. (8)) together with a coefficient of variation (Eq. (9)) and fracture development index (Eq. (10)) (Wu et al. 2016) as,

$$\rho = \frac{l_l}{S_B} = \frac{\sum_{i=1}^{n} l_i}{S_B} \tag{7}$$

$$D = -\lim_{\varepsilon \to 0} \frac{\ln N(\varepsilon)}{\ln \varepsilon} \tag{8}$$

$$V_K = \frac{\sigma}{\bar{l}} \tag{9}$$

$$f = \rho \cdot DV_K \cdot 100 = \lim_{\varepsilon \to 0} \frac{\ln N(\varepsilon)}{\ln \varepsilon} \cdot \frac{\sum_{i=1}^{n} l_i}{S_B} \cdot \frac{\sigma}{\bar{l}} \cdot 100 \tag{10}$$

where, ρ is the area density of fractures, μm^{-1}; $\sum_{i=1}^{n} l_i$ is the cumulative fracture length of the fracture, μm; S_B is the unit area, μm^{-1}; D is the fractal dimension of micro-fractures per unit area, dimensionless; V_K is the coefficient of variation of the micro-fracture suture length, dimensionless;σ is the standard deviation of the micro-fracture suture length, μm; is the average length of the micro-fracture suture, μm; and f is the microfracture development index.

3. Mechanical simulation

With the structure of the aggregate defined, inclusive of mineral and fracture heterogeneity, we present a mathematical basis for building stress distributions and recovering effective medium properties for shales of a spectrum of compositions. The aggregates are constructed from the results of the MLA analysis to define the impact of mineralogy and fracture architecture on response to applied stresses.

3.1. Mathematical methods

3.1.1. Finite element analysis

The internal deformation of a reconstructed aggregate may be determined from its pointwise reconstruction as a finite element mesh under the complex action of applied external stresses and displacements. The aggregate is represented by a mesh of triangular or quadrilateral elements comprising the mesh and solved in

2D. Stresses may be linked to strains through the constitutive relation,

$$\underset{(3\times 1)}{\boldsymbol{\sigma}}{}_{x,y,z}=\begin{bmatrix}\sigma_{xx}\\ \sigma_{yy}\\ \tau_{xy}\end{bmatrix}=\frac{E}{1-\mu^2}\begin{bmatrix}1\&\mu\&0\\ \mu\&1\&0\\ 0\&0\&\frac{1-\mu}{2}\end{bmatrix}\begin{bmatrix}\varepsilon_{xx}\\ \varepsilon_{yy}\\ \gamma_{xy}\end{bmatrix}=\underset{(3\times 3)}{\boldsymbol{B}}=\underset{(3\times 1)}{\boldsymbol{\varepsilon}} \tag{11}$$

Where $\sigma_{xx},\sigma_{yy},\tau_{xy}$ are the normal and tangential stresses linking strains,$\varepsilon_{xx},\varepsilon_{yy},\gamma_{xy}$ through the local modulus, E, and Poisson ratio, μ. This includes the elastic constitutive matrix $\boldsymbol{B}$ for the plane stress problem with the boundary conditions for the finite element analysis divided into either displacement or force/stress boundary conditions. The displacement boundary condition $BC_{(u)}$ is defined as,

$$u(x,y)|_{x=x_0,y=y_0}=\bar{u} \tag{12}$$

$$v(x,y)|_{x=x_0,y=y_0}=\bar{v} \tag{13}$$

External force boundary conditions $BC_{(p)}$ are defined as,

$$n_x\sigma_{xx}(x_0,y_0)+n_y\sigma_{xy}(x_0,y_0)=\bar{p}_x \tag{14}$$

$$n_x\tau_{xx}(x_0,y_0)+n_y\sigma_{xy}(x_0,y_0)=\bar{p}y \tag{15}$$

Where n_x, n_y are the directional cosines of the normal to the boundary *and*(x_0,y_0) are the coordinates on the boundary with, representing the stresses (distributed forces) on the boundary in the x and y directions, respectively.

3.1.2. Maximum principal stress criterion

Mechanical damage occurs when the stress exceeds as yield criterion and fractures will extend when stresses exceed a maximum principal stress criterion. A threshold yield criterion may be defined as (Chrysakis, 1986).

$$f=\left\{\frac{\sigma_{\max}}{\sigma^a_{\max}}\right\} \tag{16}$$

where, $\sigma_{\max}$ is the maximum principal stress, MPa, $\sigma^a_{\max}$ is the maximum critical principal stress, MPa.$\sigma_{\max}=\begin{cases}0,\sigma_{\max}<0\\ \sigma_{\max},\sigma_{\max}\geqslant 0\end{cases}$, and fracture occurs when the fracture satisfies$1.0\leqslant f\leqslant 1.0+f_{tol},f_{tol}$, with a default tolerance set at 0.05. The higher the maximum stress at the tip of the fracture under load, the easier the extension.

3.2. Model construction

3.2.1. Mineral model based on MLA results

Based on the results from the mineral deaggregation/dissociation, four mineral assemblages were modeled according to differences in mineral content (Fig. 2). An individual model is 3×2 μm in dimension with maximum $\sigma_{\max}=50$ MPa and minimum $\sigma_{\min}=40$ MPa principal stresses applied to the external contour. Mineral properties of density, modulus and Poisson ratio were set individually for each of nine minerals meshed into the model (Table 3). A total of five sections were processed using Photoshop to separate the different mineral types with MATLAB then applied to calculate the fractal dimension. Calculation results are shown in Table 3. The model maximally restores the mineral architecture, contact relationships and distribution characteristics of the minerals to provide a basis for investigating mineral morphology and degree of heterogeneity (Fig. 3).

3.2.2. Idealized mineral distribution model

We develop an idealized mineral characteristics model to further investigate the influence of mineral distribution characteristics and mineral content on mechanical properties. Individual mineral grains were subdivided into small squares 1 mil (0.0254 mm) in edge-dimension. The Longmaxi Formation shale has a high quartz content with a scattered distribution supplemented by carbonates and clay minerals locally distributed in agglomerates and with organic matter distributed in strips. Therefore, the characteristics of the distribution are also different, even where the gross mineral contents are identical. Thus, we establish a series of mineral distribution models to simulate agglomerates and distributions representing semi-encirclement, full-encirclement and random distributions (Fig. 4a). Individual cell size was set at 1 mil with loading simulating triaxial compression against fixed constraint at the base and a specified velocity of 4×10^{-6} mm/s at the top with a specified displacement of -4×10^{-4} mm and a stress of 60 MPa applied on the circumferential boundary. Stress concentrations are evaluated while varying quartz and clay mineral contents. The quartz mineral content was sequentially incremented to 30%, 40%, 50% and 60% with the clay mineral content correspondingly decremented to 50%, 40%, 30% and 20% with the proportion of supplementary minerals retained constant (7% calcite + 5% organic matter + 5% dolomite + 3% pyrite). The stress loading mode is identical to that of the mineral distribution model (Fig. 4b).

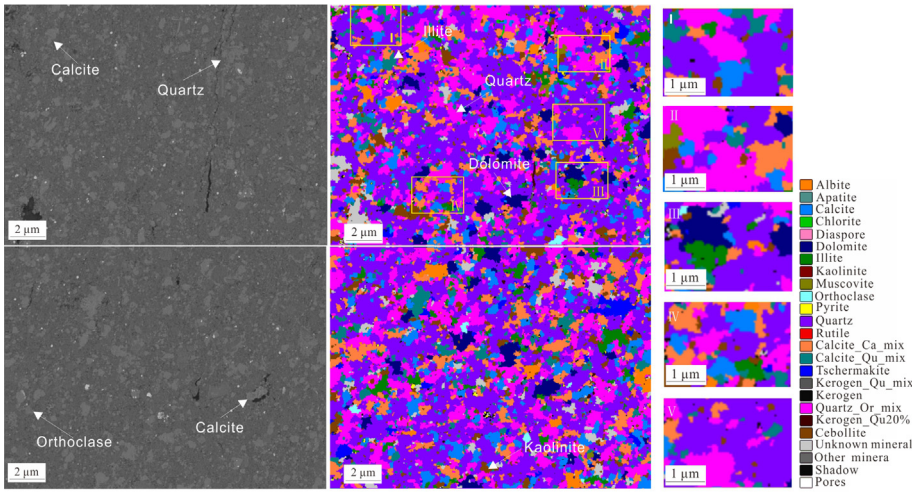

Fig. 2. Actual mineral distribution model constructed based on MLA results. On the left is mineral distribution characteristics observed under BSE. The middle is the minerals distribution characteristics after MLA. On the right are the five real mineral distribution models (I-V).

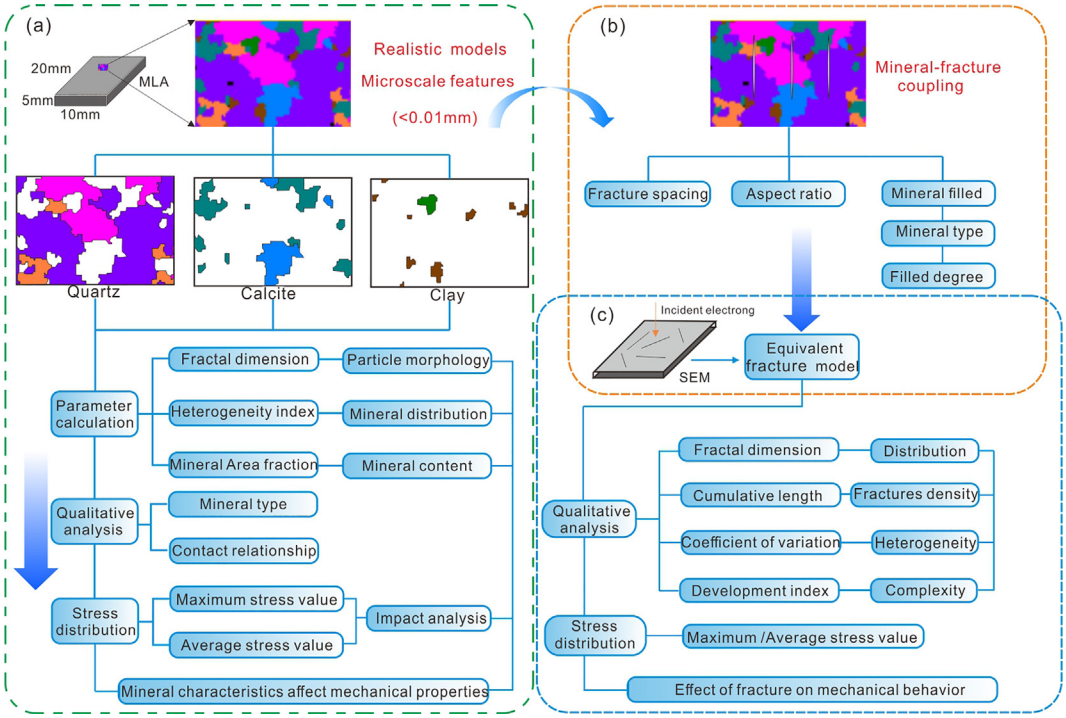

Fig. 3. Mineral model construction and idealized simulation procedures. (a) Is the analysis flow chart of mineral distribution model. Image processing uses Photoshop to extract the region of the same pixel. (b) Is the analysis flow chart of mineral fracture coupling model. Add artificial cracks to the results of MLA. (c) Is the analysis flow chart of crack model.

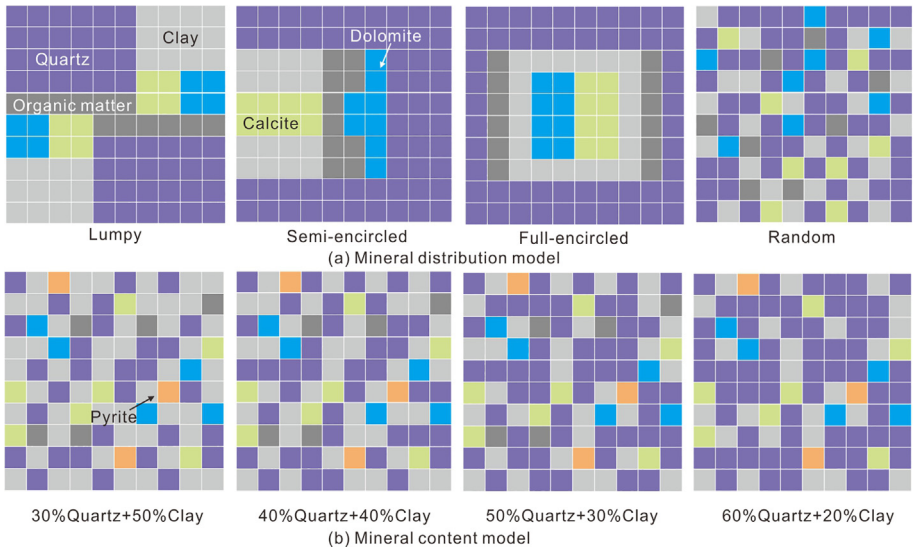

Fig. 4. Idealized mineral distribution and mineral content models. (a) Are the schematic diagram of the ideal minerals distribution model, which are lumpy distribution, semi-encircled distribution, fully-encircled distribution and random distribution respectively. And the mineral content of the models are the same, which is 48% quartz + 24% clay + 8% dolomite + 8% calcite + 12% organic matter. (b) are idealized mineral content models, the mineral contents are 30% quartz + 50% clay, 40% quartz + 40% clay, 50% quartz + 30% clay and 60% quartz + 20% clay respectively. The other minerals are 7% calcite + 5% organic matter + 5% dolomite + 3% pyrite.

The mineral contact mode model consists of three different morphologies representing point-, short-line-, and line-contacts, respectively. The mineral type was retained as quartz with a grain size of 1 mil and an applied confining pressure of 20 MPa. The grain size model was based on the point contact model by successively incrementing grain sizes with radii of 15 μm, 20 μm, 25 μm, 30 μm and 35 μm, respectively, within the same loading mode (Fig. 5a).

3.2.3. Fracture distribution model

Three-dimensional fractures are spatially unevenly distributed, morphologically complex, and difficult to quantitatively characterize. In the field of material fracture mechanics, the reduction of three-dimensional cracks to two-dimensional cracks is widely used (Tobing et al., 2016; Ly et al., 2017; Yan and Yang, 2019). Equating 3D fractures as equivalent 2D fracture traces allow the mineral MLA model to explore the combined influence stress and

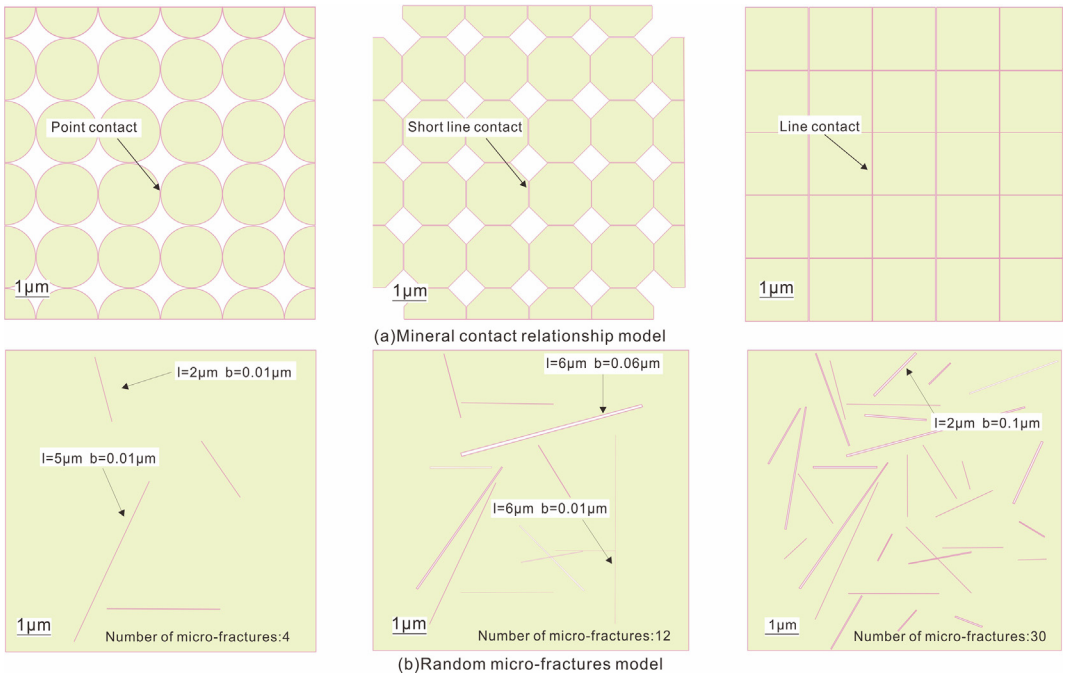

Fig. 5. Mineral contact relationship model and fracture development model. (a) Are the mineral contact relationship models. The mineral cell unit are quartz. The contact relations are point contact, line contact and short line contact. (b) Are fracture distribution models. Selected fracture lengths were in the range 1 ~ 6 μm, widths in the range 0.01 ~ 0.10 μ, and the fracture spacings set to 0.24, 0.4 and 0.48 μm.

the potential for fracture extension to be evaluated. The fracture distribution model includes fracture length, width, spacing and degree of fracture development.

Firstly, the fracture parameter model was defined from the mineral model established by MLA. The mineral encasing the fracture tip was retained constant to exclude the confounding influence of different minerals. Selected fracture lengths were in the range 1−~6 μm, widths in the range 0.01–0.10 μm, and the fracture spacings set to 0.24, 0.4 and 0.48 μm. Maximum principal stress $\sigma_H = 20$ MPa and minimum principal stress $\sigma_h = 10$ MPa were set accordingly.

Secondly, fracture variation was constrained by considering the effects of fracture area, variation coefficient and fractal dimension. Random fractures lengths were in the range 1–6 μm and widths in the range 0.01–0.10 μm, with the same load applied as in the fracture parameter model (Fig. 5b).

Thirdly, a model of fracture fill type was built to accommodate both fully-filled and half-filled fractures as defined across their width. Fill was defined as either organic matter or carbonate minerals to simulate the semi-filling type.

4. Results and discussion

4.1. Mineral composition and distribution

Here we report results from the quantitative definition of mineral compositions acquired by MLA and descriptive rendition of mineral and fracture structure recovered from SEM.

4.1.1. MLa

Mineral contents of the four samples were evaluated by MLA, with quartz, dolomite, calcite and clay minerals as the main components (Table 1). The quartz content is high and distribution continuous throughout the entire field-of-view, while the distribution of calcite is more broadly dispersed (Fig. 2). The dolomite content is relatively high and clumped in specific areas (Fig. 2) with clay minerals accounting for > 35% of all the minerals. Kaolinite and illite are generally distributed as clumps, with relatively high kaolinite contents. Mosaics of the different mineral fractions can be observed under high magnification. The contacts between different particles are described as line-, short-line- and point-contacts. The calcite particles are commonly inlaid as mosaics inside quartz particles. Micro-fracture distributions are poorly characterized by MLA, requiring that SEM was applied to define fracture morphology with the results reported in section 4.1.3 (Table 2).

Table 1
Statistics distribution of mechanical parameters for different minerals.

Mineral type	Density (g/cm^3)	Young's modulus (GPa)	Poisson's ratio
Quartz	2.65	96.25	0.069
Calcite	2.72	80.50	0.310
Muscovite	2.77	56.80	0.250
Biotite	2.70	33.80	0.270
Rutile	4.20	229.00	0.235
Organic matter (OM)	1.30	6.26	0.145
Dolomite	2.81	120.00	0.270
Pyrite	5.10	286.80	0.160
Clay minerals	1.40	43.80	0.340

Data from Shi et al., 2019; Sun et al., 2020a, 2020b; Jia et al., 2020.

Table 2
Mineral contents from MLA tests.

Samples	Mineral and organic matter compositions (%)					
	Quartz	Dolomite	Calcite	Pyrite	Clay minerals	Organic matter
1	34.7	3.6	8.2	1.4	39.3	3.9
2	30.6	19.0	2.7	1.6	35.6	2.0
3	32.3	14.2	0.8	1.5	43.1	2.0
4	27.7	3.8	10.2	0.8	44.7	3.1

Table 3
Mineral contents of the samples tested by XRD.

Samples	Mineral content (wt%)						
	Quartz	Feldspar	Calcite	Dolomite	Pyrite	Clay mineral	Others
1	36	2	11	4	3	42	2
2	29	1	4	22	2	37	5
3	31	4	2	17	2	41	3
4	29	4	13	4	1	46	3

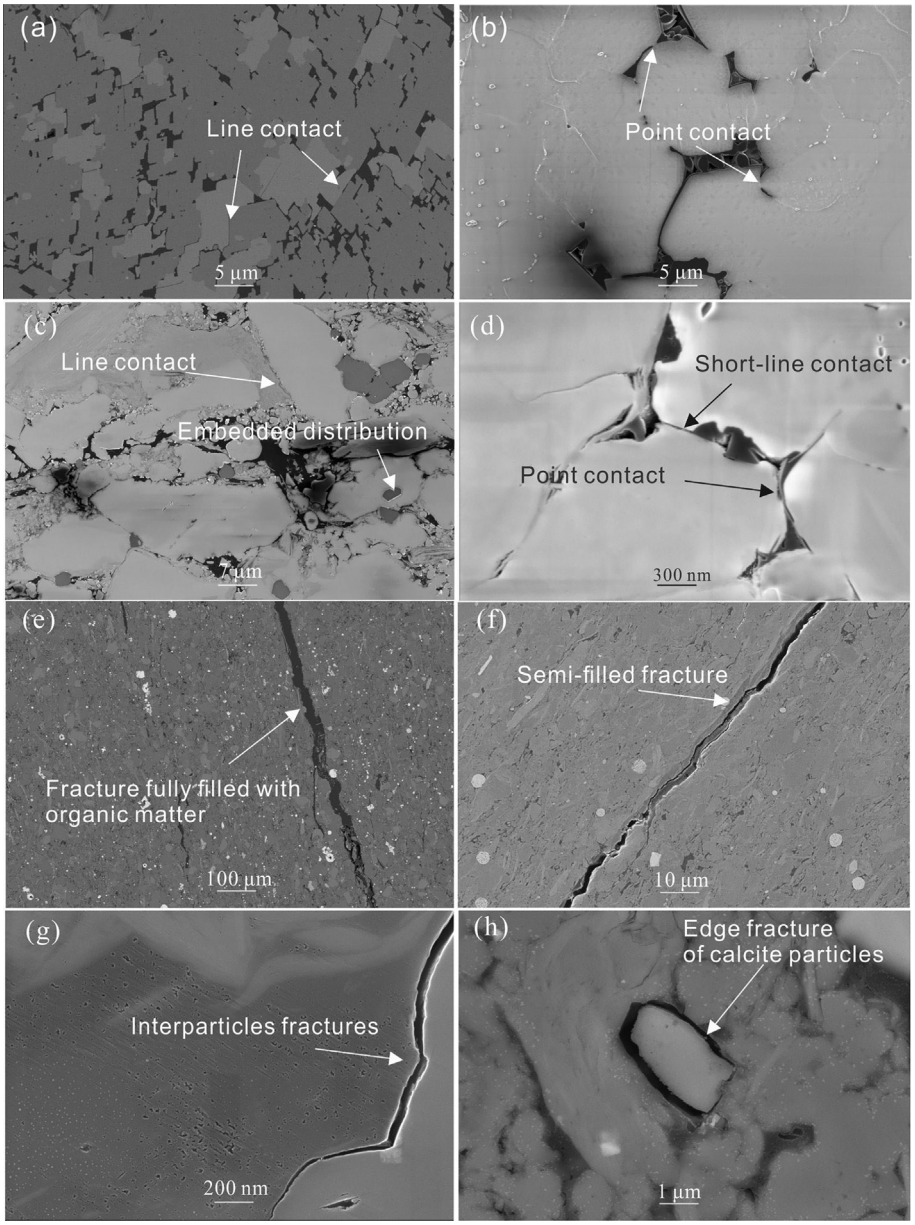

Fig. 6. Microstructure of minerals contacts and fracture extension within shales under SEM. (a-d) are the contact relationship of minerals under SEM. (e-h) is the fracture feature under SEM. The fractures are fully filled or semi-filled with organic matter. Common fractures under SEM include interparticles fractures and edge fractures of particles.

4.1.2. XRd

As the MLA results are acquired from only 2D scanned views, its representativeness to volume content must be verified by XRD (Table 3). The tested shale comprises mainly quartz, carbonate and clay minerals, with some feldspar and trace pyrite. XRD identifies quartz as almost one third of the bulk sample with ~ 40% clay minerals - both predictions similar to the MLA results.

4.1.3. SEM

The SEM results show that the mineral particles are intergrown into each other under the influence of compaction and diagenesis with some of the particle edges broken as a result of high compaction. The contact relationships can be variously classified as line- (contact length > 3 μm) (Fig. 6a), point- (contact length < 1 μm) (Fig. 6b and 6d), and short-line-contacts (contact

length 1 – 3 μm) (Fig. 6d) with all three contact modes coexist in a single view. Microfractures are well developed, including cleavage fractures, particle edge and interparticle fractures. The microfractures are mostly filled or semi-filled by organic bitumen (Fig. 6e, 6f). Particle edge fractures are mainly developed around calcite (Fig. 6h) with interparticle fractures mostly developed between gypsum aggregates (Fig. 6g). Certain parts of the microfractures are distributed inside the mineral grains or at the edges of rigid grains. Microfracture morphology may be defined as either jagged or linear, with a wide range of sizes. The length of microfractures is 3–50 μm and the width of microfractures is 20 nm–1 μm.

4.2. Mineral influence on stress distribution

The reaction of the shale samples to stresses is reported here as related to the actual and idealized models of mineral distribution. Mineral distribution morphologies are described as clumped, semi-circular, full-encircled and randomly distributed.

4.2.1. Mineral distribution

The compositions of these shales are mainly siliceous, carbonate and clay with smaller amounts of high-density minerals. The siliceous minerals are brittle and easily fractured under load and are mainly represented by quartz and feldspar. The XRD results confirm the high proportional content of these minerals. Calcite and dolomite are typical carbonate minerals. And they have an important influence on the brittleness of shale. The mechanical properties of the carbonate minerals are similar to those of quartz and with higher modulus and density for the dolomite. The clay minerals include illite, kaolinite, chlorite and mixed-layer illite. Organic matter and clay minerals are characterized by low Young's modulus and density (Table.3). These minerals exhibit plasticity

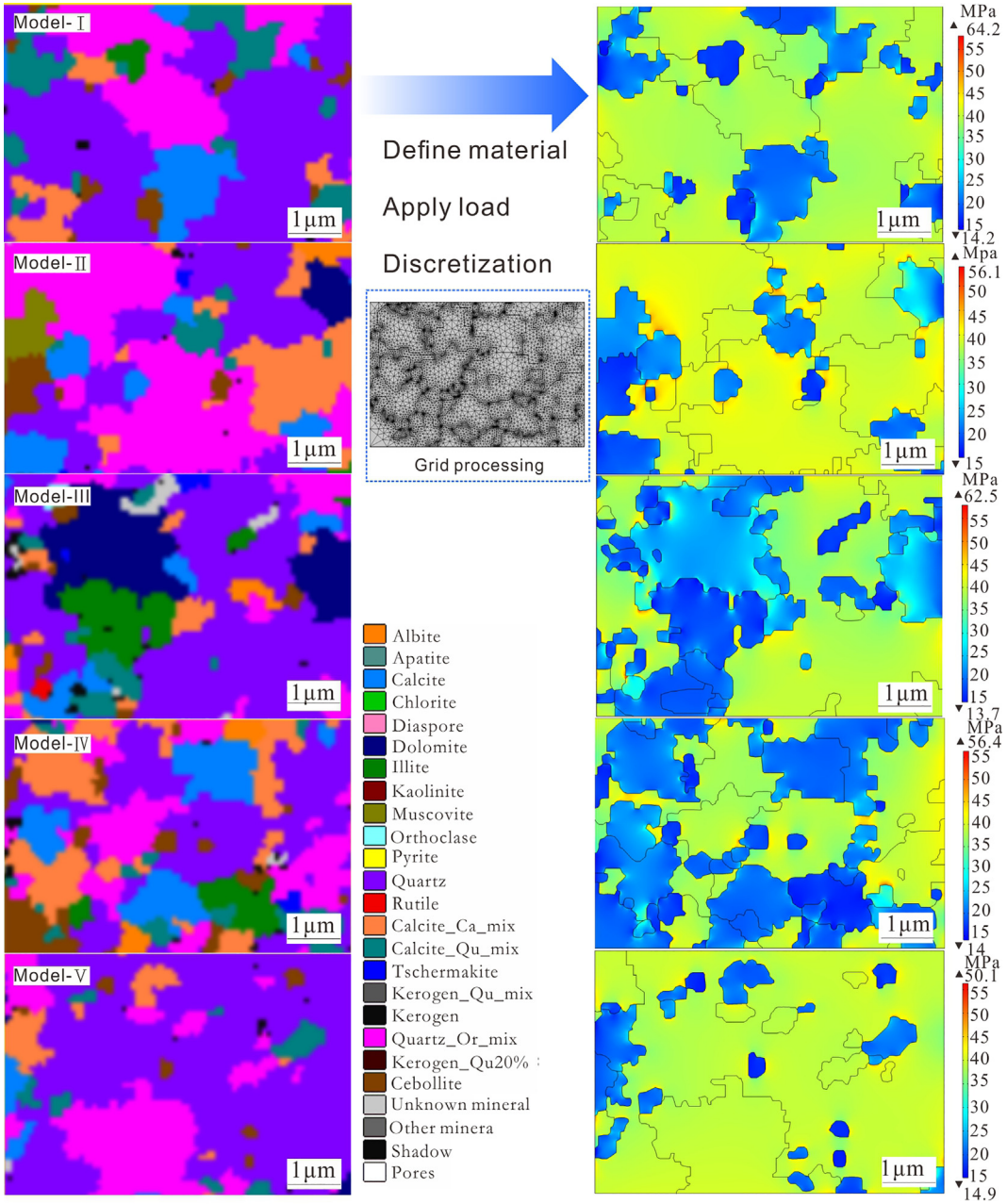

Fig. 7. Stress distribution of mineral model based on MLA results. On the left are the five real mineral distribution models (I-V). On the right are the stress distribution of the models under load with maximum $\sigma_{max} = 50MPa$ and minimum $\sigma_{min} = 40MPa$ principal stresses applied to the external contour.

under load. The stress concentrations within quartz is the highest and exert a significant effect on the mechanical properties of the shale (Fig. 7).

The stress concentration is significantly influenced by the distribution of minerals. This is weakest when the brittle minerals are distributed in clumps (Fig. 8a) and brittle damage is less likely to occur as the clumped distribution effectively increases the effective grain size. The stress concentration is strongest when the brittle minerals are randomly distributed with the maximum stress concentration located at the diagonal contact between brittle minerals. XRD and MLA results both indicate that the shale contains a small amount of high-density minerals - including pyrite and heavy minerals. The Young's modulus of pyrite is three times that of quartz, and that of rutile is two to three times that of quartz (Table 3). Both pyrite and rutile are also more dense than quartz with a brittleness index significantly higher than that of clay minerals and organic matter. However, the content of high-density minerals is generally low, with pyrite present at 0.3% to 16.9% (Xu et al. 2021), although it can play an outsized role in increasing brittleness.

The maximum stress concentration increases significantly with increasing quartz content (Fig. 8b). Moreover, there is a positive correlation between quartz content and fractal dimension (Fig. 9a). The high quartz content corresponds to the increase in quartz particle size and perimeter, and the fractal dimension of particle size also tends to be increased. The simulations results show that the higher degree of quartz heterogeneity can result in high stress concentrations (Fig. 9b). Generally, the high quartz content favors the occurrence of brittle damage. However, when the quartz content is much higher, e.g., 75% quartz content, the stress concentration decreases slightly (see Fig. 9c). The higher quartz fractal dimensions is also approving to stress concentrations (Fig. 9d), leading to brittle failure. However, when the quartz content is much too high, although the fractal dimension increases and its particle morphology tends to be complex, the degree of heterogeneity will be correspondingly significantly reduced. Thus even though the particle size increases, it is not conducive to stress concentration (see Fig. 8d, 8g). The stress maximum of carbonate minerals is second only to quartz, while the variation trend is similar to that of quartz (Fig. 9e, 9f).

The Young's modulus of dolomite is higher and it is more brittle than calcite, and the stress concentration of dolomite under load is more obvious than that of calcite. There is an obvious stress mutation in model-III (Table 4). It contains a small amount of rutile. And, rutile has the characteristics of high density and high hardness, and the young's modulus is much greater than that of quartz. When it is in contact with other minerals such as quartz under load, it easily forms a higher stress concentration zone at the contact point. Thus, the surrounding minerals tend to be damaged as the stress reaches the damage strength. Furthermore, the content of dolomite of the model is high. Dolomite, which is more brittle than calcite, accounts for 67% of the carbonate mineral content.

Under certain load, the stress concentration of clay minerals is weak, but a small amount of clay minerals is beneficial to improve the contact relationship of shale minerals and enhance the degree of heterogeneity of brittle minerals. Once the clay mineral content exceeds 7%, the maximum stress value decreases rapidly by the influence of mineral content (Fig. 9g). The average stress value of shale also decreases with the increase of clay mineral content and fractal dimension (Fig. 9j).

4.2.2. Mineral contact relationships

The simulation results indicates that the maximum stress concentration on the minerals decreases exponentially with the increment of mineral particle sizes (Fig. 9i). The stress value of point contact is the most evident (Fig. 10), conducive to brittle damages. The quartz particles possess a hexagonal crystal shape and are mostly randomly distributed under the microscope. The contact relationship between the quartz grains are mainly of point and short line contacts. Thus, small quartz grains are more susceptible to be damaged than large quartz grains.

As indicated by Hertzian contact theory, the smaller the contact point area between particles, the higher stress concentrations generally occurs (Kachanov et al., 1994; Neto et al. 2011). The contact area between small minerals particles is limited, easily forming point contacts, and consequently forming higher stress concentration. Smaller grained minerals also beneficial to lower energy dissipation during fracturing fluid expansion (Shimizu et al., 2011; Huang et al., 2021). Sun et al. (2020a, 2020b) counted the equivalent diameter and number of high-density brittle minerals in shale and found that the equivalent diameter of brittle mineral particles was mainly at the micron level. And the equivalent diameters of more than 90% of brittle mineral particles is between 200 and 800 μ. The quartz content in models IV and V are as much as

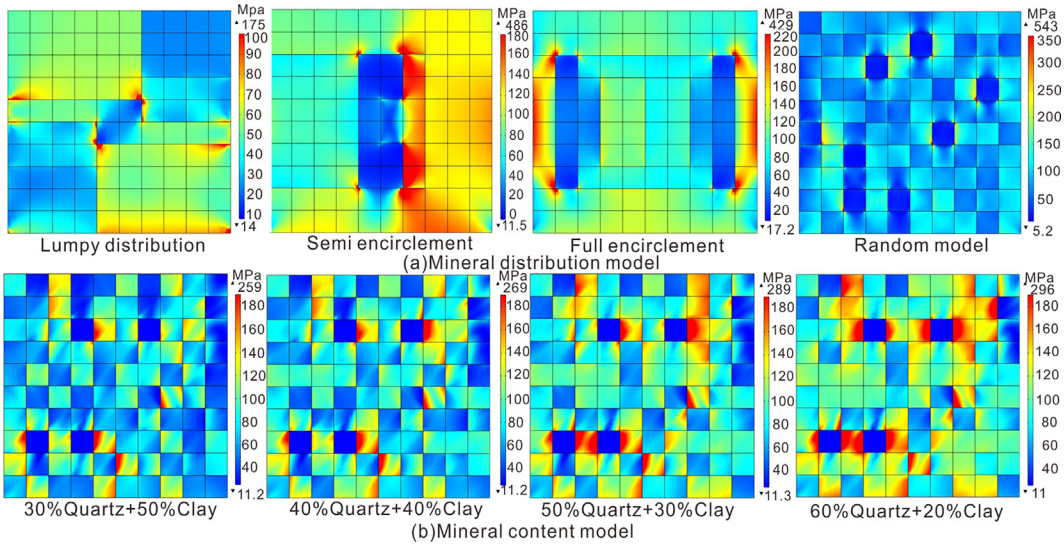

Fig. 8. Effect of mineral distribution and content under stresses. Fig. 8 shows the simulation results of Fig. 4 under the load of the model, which condition is with loading simulating triaxial compression against fixed constraint at the base and a specified velocity of 4×10^{-6} mm/s at the top with a specified displacement of -4×10^{-4} mm and a stress of 60 MPa applied on the circumferential boundary.

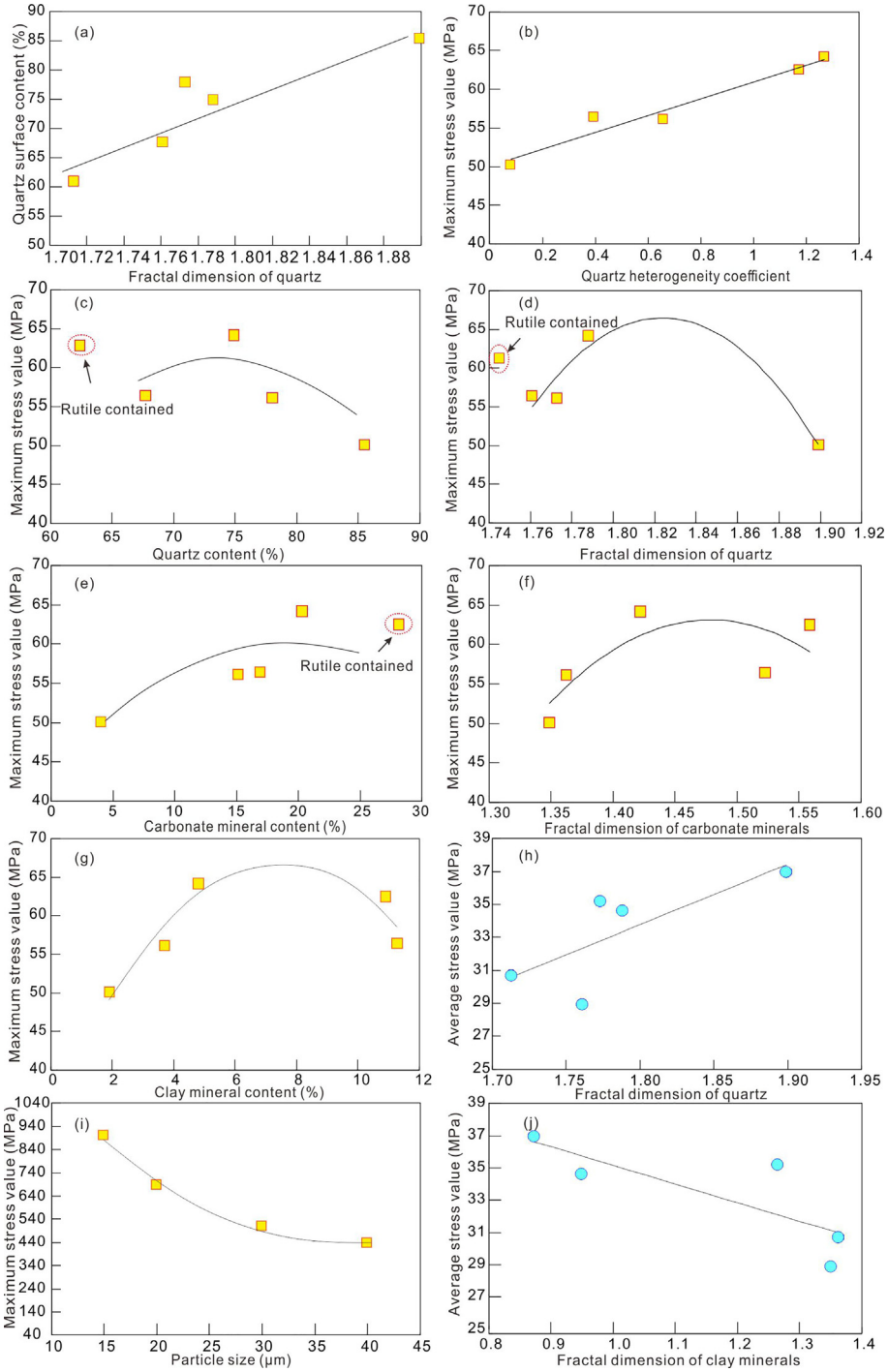

Fig. 9. Effect of mineral characteristic parameters on stress concentration. (a) It is the relationship between fractal dimension of quartz and mineral content. (b-g) are the correlation between the maximum stress value of model (I-V) under load and micro mineral characteristics. (i) Is the correlation between the maximum stress value and particle size under load. (h) and (f) are the relationship between the average stress value of the models and the mineral content of calcite and clay.

78% and 85.5%, respectively, which is higher than the quartz content in model I (74.9%) (Fig. 7). However, the maximum stress concentrations are slightly lower for the slices with high quartz content. A reason is that the mineral composition in models IV and V tends to be homogeneous. For relatively low brittle minerals, if their content exceeds certain contents, e.g., carbonate and clay minerals reach 18% and 7% separately), the stress concentration decreases (Fig. 9e, 9g). Thus, temperate contents of quartz, carbonate and clay minerals all acting on the brittleness and stress reactions.

4.2.3. Mineral particle morphology and heterogeneity degree

For rocks with similar mineral contents, the more complex the mineral structures, the higher the fractal dimensions are. Fractal dimension show similar influences on the mechanical properties as mineral contents. When the fractal dimensions exceed a certain value, the maximum stress concentration decreases. This is also influenced by the variation of particle sizes and contact modes (Fig. 9d, 9f). The average stress concentrations influence on the shale is significantly affected by the mineral content differentiations. As the fractal dimension of quartz increases, the average

Table 4
Mineral content and mineral fractal statistics of MLA model.

Number	Mineral surface content (%)					Fractal dimension of mineral particles			mechanical property	
	Quartz	Calcite	Dolomite	Kaolinite	Illite	Quartz	Calcite	Kaolinite	$\bar{\varepsilon}$/GPa	$\bar{\upsilon}$
I	74.9	20	/	3.5	1.3	1.7879	1.4218	0.9485	90.529	0.128
II	78.0	11	3.8	3.7	/	1.7728	1.3468	1.1513	91.350	0.121
III	61.0	9	18.8	2.2	8.7	1.7127	1.3200	0.9603	92.763	0.178
IV	67.7	17	/	5.1	4.6	1.7607	1.5225	1.2338	84.410	0.190
V	85.5	4	0.34	1.9	/	1.8990	1.3485	0.8718	93.226	0.101

Note: $\bar{\varepsilon}$, average Young's modulus, GPa; $\bar{\upsilon}$, average Poison's ratio.

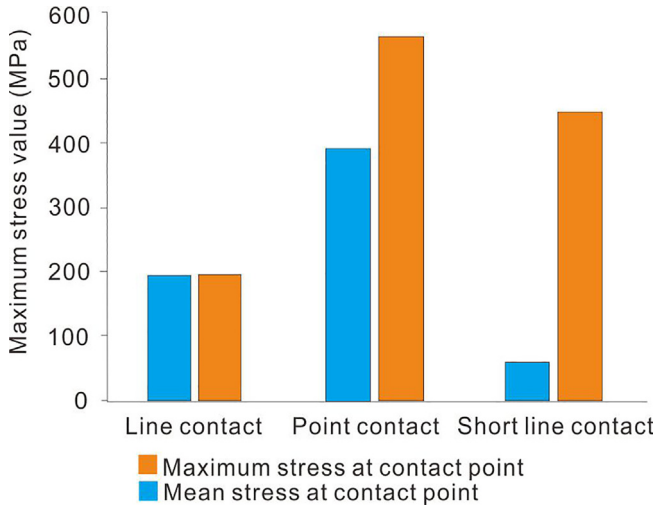

Fig. 10. Effect of mineral contact modes on stress concentration. Contact modes include point contact, line contact and short-line contact.

stress concentration continuously increases (Fig. 9h), thus the shale as a whole is of a higher stress state. The increment of clay mineral fractal dimensions and clay contents both decrease the average stress concentrations (Fig. 9j). The brittle mineral particles are often accompanied by weak contact surfaces between grains, and the hydraulic fractures are easy to cross the inter-grain interfaces and induce complex fractures in the process of reservoir modification. Therefore, the fractal dimension of brittle minerals can also characterize the ability of complex microfracture generation within shale.

The mineral heterogeneity index is adopted to characterize the heterogeneity of minerals distribution. The calculated quartz heterogeneity coefficients of the five models are 1.27, 0.66, 1.17, 0.39 and 0.08 for I to V. The maximum stress concentrations are proportional to the quartz heterogeneity coefficient. The stronger the distribution heterogeneity of brittle minerals, the more favorable for brittle damage.

The reaction of shale to compression is influenced by the specific minerals content, minerals particles contact relationship and distribution patterns. The brittleness of shales with low brittle minerals is mainly influenced by the content of plastic clay

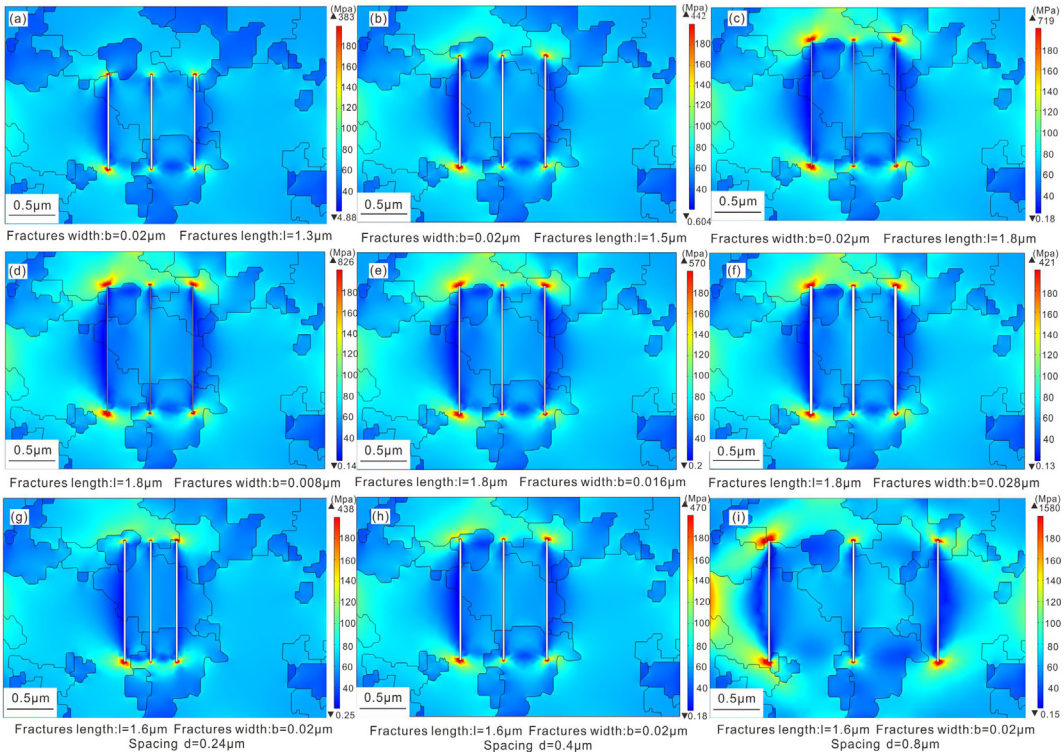

Fig. 11. Stress distribution under different fracture morphology. (a-c) are the fractures length models. The fracture length is 1.3 μm, 1.5 μm, 1.8 μm respectively. (d-f) are the fractures width models. The fracture width is 0.008 μm, 0.016 μm, 0.028 μm respectively. (g-i) are the fractures spacing models. The fracture spacing is 0.24 μm, 0.4 μm, 0.8 μm respectively.

minerals and mineral contacts. When the content of certain brittle minerals is particularly high, e.g., quartz > 75%, the influence of contact relations and grain size increases significantly. For shales with similar mineral compositions, the particle morphology and heterogeneity degree influence the mechanical responses. Quartz with complex morphology and high heterogeneity degree is favorable to brittleness damage.

4.3. Fracture influence on stress distribution

The stress distribution influenced by fractures morphology, fracture filling status and fracture complexity is reported here, as well as interactions between parallel and random distributed fractures.

4.3.1. Fracture morphology

The simulated fracture morphological characteristics include fracture length, width, and aspect ratio. Fracture influences on the stress concentration is much higher than the minerals (Fig. 11). When fractures exist in the shale, the stress is mainly concentrated at both ends of the fractures. And both the maximum and average stress concentrations under long fractures are more obvious than that of the short fractures (Fig. 12a). If the stress at the ends is higher than the maximum critical stress valueσ_{max}, the fracture extends. The fracture width is negatively correlated with the stress concentration, and the wider the fracture is fractured, the less likely it is to be extended (Fig. 12b, 13b). The higher the fracture aspect ratios are, the narrower and longer the fractures tend to be. And the stress concentration at both ends under load is more significant (Fig. 12c, 13c). Thus, precursor higher aspect ratio fractures is conducive to fracture length extension.

The SEM results show that the fractures are mostly filled with carbonate minerals or organic bitumen, and the filling state can be divided into fully filled and semi-filled (Fig. 6e, 6f). When the fractures are semi-filled, the fractures width becomes narrower with aspect ratio increment, thus the fractures are prone to extension (Fig. 14). And fractures saturated with brittle minerals, e.g. carbonate while not bitumen, are more easily to be extended.

4.3.2. Fracture complexity

The fracture complexity is determined by the morphology, heterogeneity and their spatial distributions. The fracture heterogeneity is characterized by the variation coefficient of fracture length, which is directly related to the fracture growth. Both maximum stress and average stress concentration is positively related to the fracture length variation coefficient (Fig. 12d, 13d). As with the increment of fracture fractal dimensions, the maximum concentration values show a wide variation range. And under high fractal dimensions, the maximum concentrations slightly decrease (Fig. 12e). The increase of fractal dimensions in the early stages is accompanied by the fracture complexity increase in spatial, thus the stress concentrations are high. As with the increment of fractal dimensions, which also means that the number of fractures increase, with consequently decreasing the fracture spaces. Thus, the stress can work on the internal fractures while not only the external ones, the maximum stress values decrease (Fig. 12e).

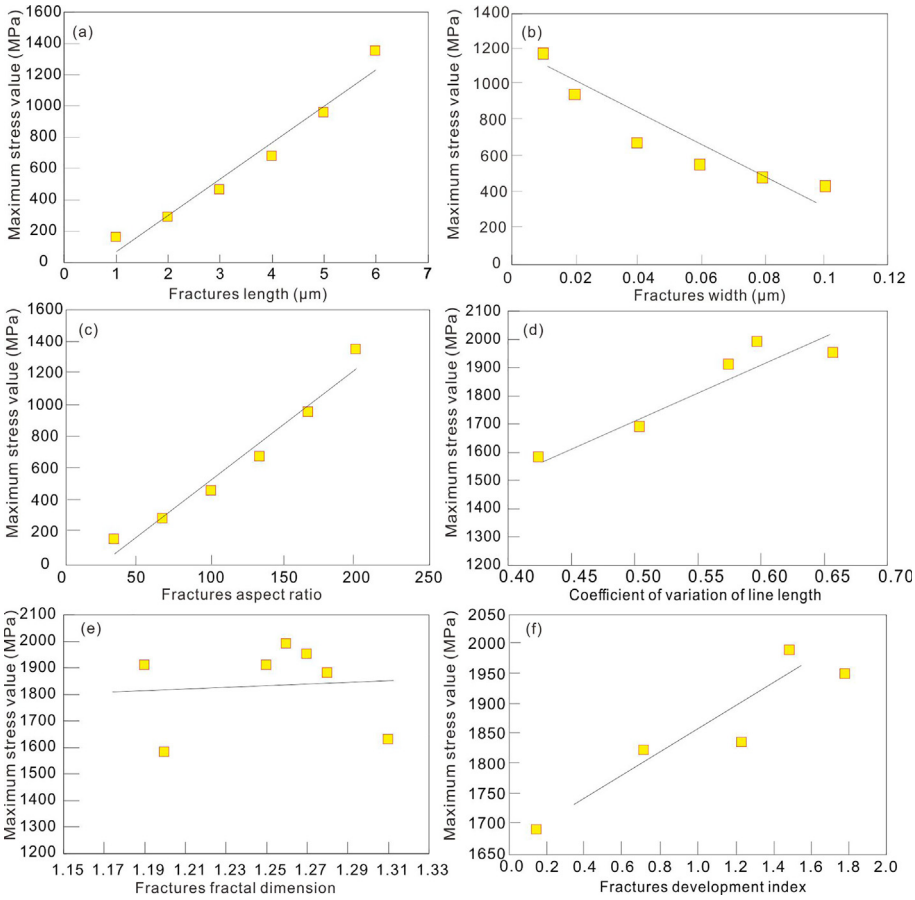

Fig. 12. Influence of fracture parameters on the maximum stress concentrations values. (a-c) are the relationship between the fractures size parameter models and the maximum stress value under load. (d) Is the relationship between the maximum stress value and variation coefficient under load. (e) Is the relationship between the maximum stress value and crack spacing under load. (f) Is the relationship between the maximum stress value and fracture development index under load. The stress condition is maximum $\sigma_{max} = 50MPa$ and minimum $\sigma_{min} = 40MPa$ principal stresses applied to the external contour.

However, the average stress values show a continuous increment (Fig. 13e). The effect of fracture development index f shows both positive influences on the maximum and average stress concentrations (Fig. 12f, d 13f). Similar to the fractal dimensions, the maximum stress concentration will also decrease as with much more fractures being developed.

4.4. Shale physical model construction optimization

The content and orientation of clay minerals and kerogen are important parameters influencing shale anisotropy (Ding et al., 2020; Du et al., 2020; Panizza and Ravazzoli, 2019; Zhou and Zhao, 2020). Shale petrophysical models are usually built based on the clay minerals compositions, combined with SEM and other image technology to acquire the microstructure. The accuracy of the petrophysics models is being continuously improved by combination of mathematical and new physical detection methods. Vernik and Nur (1992) established a petrophysical model of transversely isotropic sbale Based on Backus averaging theory. Hornby et al. (1994) derived anisotropic SCA and DEM models from isotropic SCA model and differential equivalent DEM model. Gaussian distribution based on SEM results were also introduced to simulate the directional arrangement and stratification of clay and kerogens. Subsequently, the anisotropic SCA and DEM models was also used to refine the petrophysical models by considering brittle minerals, pore types, and particle aspect ratios, et al (Fig. 15).

Petrology and rock physical properties both control the mechanical responses of shale under stresses (Zhao and Zhang, 2020). The above studied results show that the mineral distributions, particle morphology and contact relationships all significant influences its stress responses. The stress concentrations of shales with low brittle minerals are mainly influenced by the content of hard particles, e.g., quartz, feldspar, etc. Shales with moderate brittle mineral content are still dominated by the percentages of fragile minerals content. However, the effect of clay minerals and brittle mineral under stresses is significantly weakened. At this time, the effect of mineral particle morphology (fractal dimension,

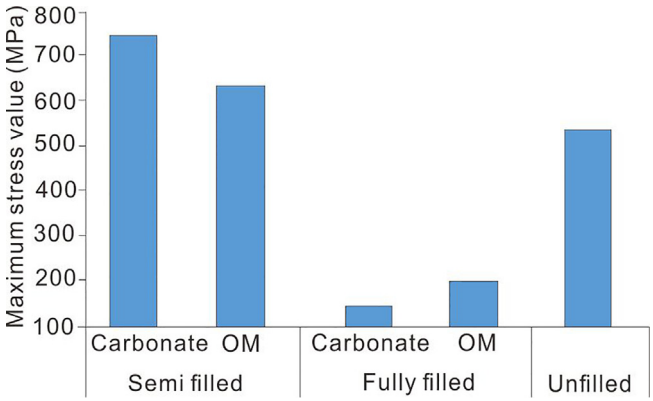

Fig. 14. Effect of fracture filled on stress concentrations. Filled modes are divided into fully filled, semi filled and unfilled. The types of minerals filled include carbonate and organic matter.

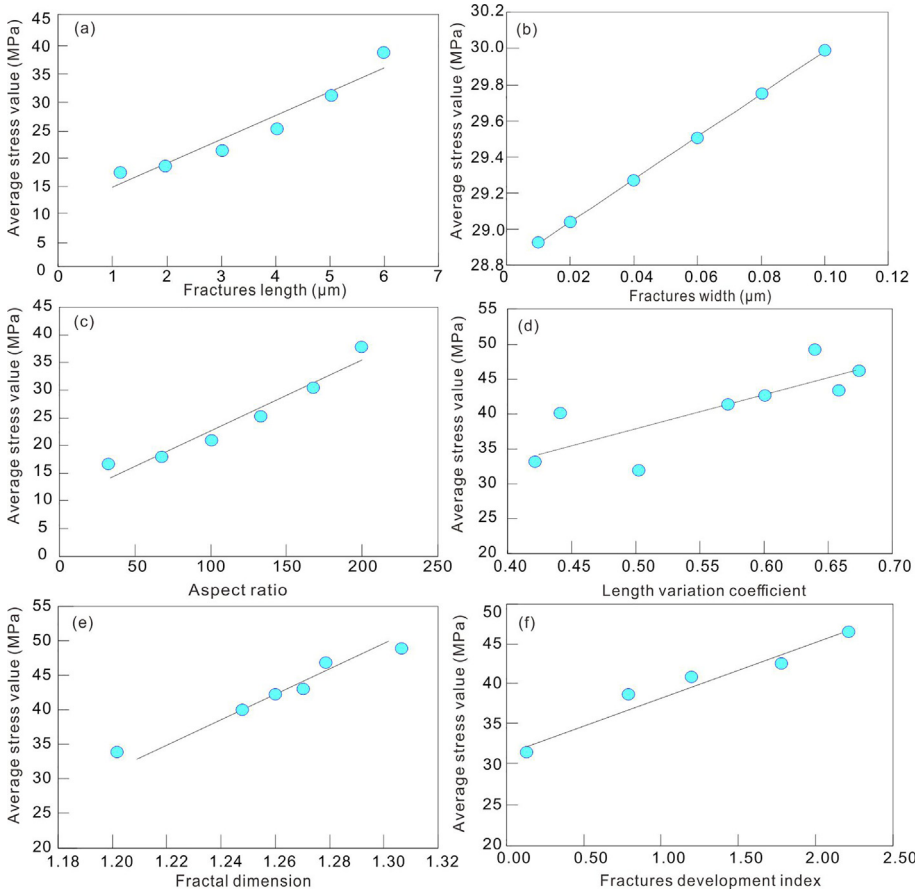

Fig. 13. Influence of fractures parameters on average stress concentration values. (a-c) are the relationship between the fractures size parameter models and the average stress value under load. (d) Is the relationship between the average stress value and variation coefficient under load. (e) Is the relationship between the average stress value and fractures spacing under load. (f) Is the relationship between fracture fractal dimension and average stress value under load. The stress condition is maximum $\sigma_{max} = 50\,MPa$ and minimum $\sigma_{min} = 40\,MPa$ principal stresses applied to the external contour.

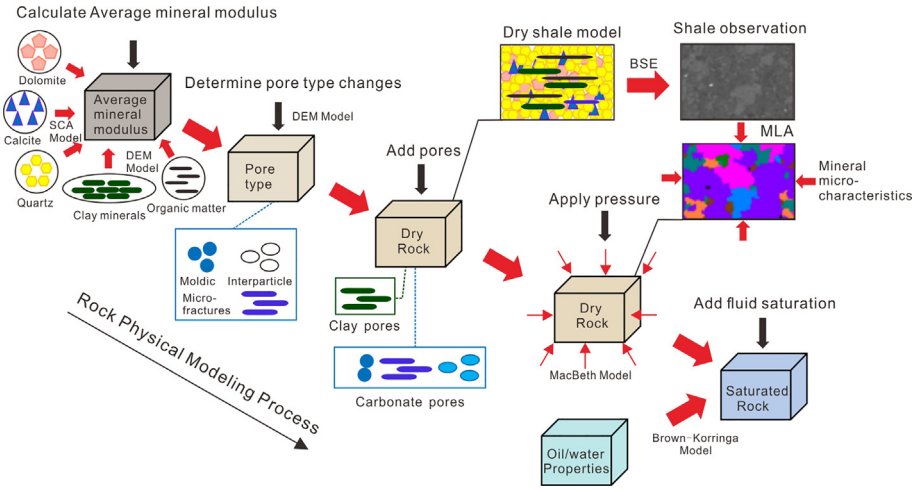

Fig. 15. Petrophysical modeling process considering mineral contacts (Hu et al., 2013).

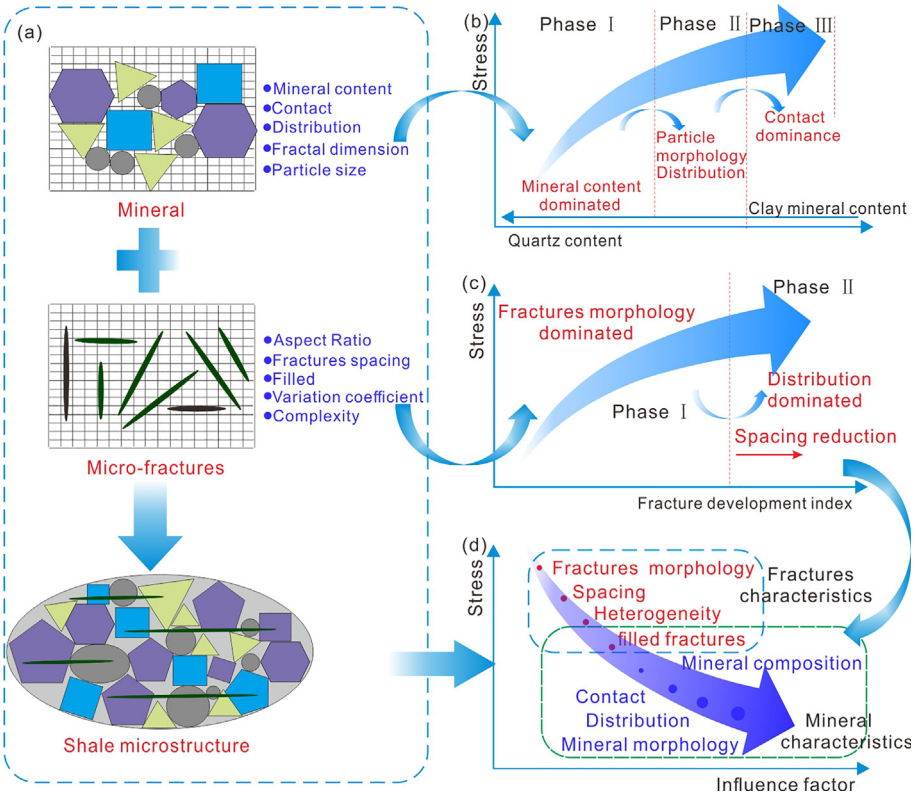

Fig. 16. Microscopic characteristics and mechanism of shale under stress. (a) Shale composition diagram. Shale is composed of mineral and fracture system. (b) Main controlling factors of stress concentration under different mineral content. (c) Main controlling factors of stress under different fracture development degrees. (d) Comparison of effect of shale microscopic characteristics on stress concentration.

particle size, etc.) and distribution modes (heterogeneity, etc.) are enhanced. For shales with certain high brittle minerals, e.g. > 75% quartz content, contact relations between the mineral particles dominate its stress reaction. The stress concentrations are significantly higher for short line and point contact conditions compared to line contacts (Fig. 16b).

The effect of fractures on stress values is related to its development degrees. When a small number of micro-fractures are developed, the size of the fractures plays a dominant role. Fractures with narrow shapes have higher stress concentrations at the fracture tips. When a large number of fractures exist, the distribution pattern, variation coefficient, and fracture spacing show prevailing role on the stress reactions. Compared to fractal dimensions and variation coefficient, the effect of fractures spacing is more obvious. Under high stresses, mutual transfer of tips stress may happen between two close fractures. On the whole, the role of fractures is more important than that of the minerals (Fig. 16d). These theoretical results can provide guidance for petrophysical modeling of shale oil and gas reservoirs.

5. Conclusions

We develop a model to faithfully reconstruct the content and structure of mineral aggregates containing microfractures. We use the reconstructions to develop meshed finite element models

and examine mechanical response to loading to define equivalent medium properties. We draw the following conclusions from this study.

(1) Based on MLA and finite element simulations, high-fidelity models honoring mineral distributions in real shales may be effectively (re)constructed. Stress distributions may be defined under different loading magnitudes and obliquities with real mineral distributions simulated. These enable the impacts on mechanical response of mineral content, topology, mineral contact characteristics and particle size to be determined. In addition, models containing random fractures are established based on the morphological characteristics of the fractures and as driven by stress concentrations for any given fracture morphology, heterogeneity and spatial distribution.

(2) These mineral composition models show that higher contents of brittle minerals (e.g., quartz, dolomite and calcite) result in elevated stress concentration around fractures with the potential for fracture extension. High density minerals (e.g., rutile), although typically present in small proportions, can also play an important role in increasing brittleness. The stress concentration for shale reconstructed as a block distribution of minerals is the lowest with a random distribution with high heterogeneity most conducive to brittle damage. Point- and short-line-contacts return higher stress concentrations than longer line-contacts.

(3) Idealized minerals distribution models show that the content of brittle minerals, the structure of the mineral aggregate and grain-grain contact model all control the stress distribution. Even low concentrations of brittle minerals (e.g., quartz, feldspar and calcite) control the stress distribution. As the content of brittle minerals increases the impacts of particle size and modes of distribution and compaction diminish the former controlling role of mineral content. Particle morphology and the form of contact exert major influence at much higher contents of brittle minerals.

(4) Idealized fracture distribution models show that both fracture size and aspect ratio are the two key factors controlling stress concentration if the number and density of fractures number are limited. For shales with increasing number density of fractures, fracture aperture, fractal dimension and heterogeneity exert important influence on the mechanical response. The magnitude of stress concentrations is more sensitive to the presence of fractures than the presence of minerals for a given loading condition. Moreover, the fractures can transfer stress to surrounding fractures under conditions of high stress.

Declaration of Competing Interest

The authors declare that they have no known competing financial interests or personal relationships that could have appeared to influence the work reported in this paper.

Acknowledgements

This study was supported by the National Natural Science Foundation of China (Grant No. 42072194, U1910205), the Fundamental Research Funds for the Central Universities (800015Z1190, 2021YJSDC02). We would like to thank the reviewers for their good comments and suggestions in improving the manuscript.

References

Anastasia, G.I., Jason E.H., I. Yucel, A., L. Taras, B., David, R.C., Yousif K., K, Timothy, J. K., Kitty, L.M., Laura, J. P., Roberto, S., 2017. Shales at all scales: Exploring coupled processes in mudrocks. Earth-Sci Rev. 166, 132-152.

Arif, M., Mahmoud, M., Zhang, Y., Iglauer, S., 2020. X-ray tomography imaging of shale microstructures: A review in the context of multiscale correlative imaging. Int. J. Coal Geol. 233, 103641.

Ban, Y., Fu, X., Xie, Q., 2020. Revealing the laminar shale microdamage mechanism considering the relationship between fracture geometrical morphology and acoustic emission power spectrum characteristics. B. Eng. Geol. Environ. 79, 1083–1096.

Bandyopadhyay K., 2009. Seismic anisotropy: Geological causes and its implications to reservoir geophysics. Stanford University.

Chen, S., Shi, X., Bao, H., Gao, L., Wu, J., 2021. Experimental study of shale drillability with different bedding inclinations under varying wellbore pressure conditions. J. Pet. Explor. Prod Te. 11 (4), 1751–1759.

Chrysakis, A.C., 1986. A new criterion of mixed-mode fracture propagation based on the maximization of principal stress σ1. Eng. Fract. Mech. 24 (3), 361–369.

Davis, S.H., Moin, P., 2016. Mechanics of hydraulic fractures. Annu. Rev. Fluid Mech. 48, 311–339.

Deng, X., Liu, C., Guo, Z., Liu, X., Liu, Y., 2019. Rock physical inversion and quantitative seismic interpretation for the Longmaxi shale gas reservoir. J. Geophys. Eng. 16 (3), 652–665.

Ding, P., Wang, D., Gong, F., Wang, L., Li, X., 2020. Laboratory observation of velocity anisotropy affected by clays and microfractures in artificial clay-rich shale samples. J. Petrol. Sci. Eng. 191, 107156.

Du, H., Radonjic, M., Chen, Y., 2020. Microstructure and micro-geomechanics evaluation of Pottsville and Marcellus shales. J. Petrol. Sci. Eng. 195, 107876.

Falahat, R., Farrokhnia, F., 2020. Rock physics modelling of the carbonate reservoirs: A log-based algorithm to determine the pore aspect ratio. J. Appl. Geophys. 173, 103930.

Fan, M., Han, Y., Tan, X., Fan, L., Gilliland Ellen, S., Ripepi, N., Chen, C., 2021a. Experimental and numerical characterization of lower huron shale as a heterogeneous material. Rock Mech. Rock Eng. 54 (8), 4183–4200.

Fan, X., Luo, N., Liang, H., Sun, H., Xie, L., 2021b. Dynamic breakage characteristics of shale with different bedding angles under the different ambient temperatures. Rock Mech. Rock Eng. 54 (6), 3245–3261.

Gholami, R., Elochukwu, H., Fakhari, N., Sarmadivaleh, M., 2018. A review on borehole instability in active shale formations: Interactions, mechanisms and inhibitors. Earth-Sci. Rev. 177, 2–13.

Guo, P., Li, X., Li, S., Yang, W., Wu, Y., Li, G., 2021. Quantitative analysis of anisotropy effect on hydrofracturing efficiency and process in shale using X-ray computed tomography and acoustic emission. Rock Mech. Rock Eng. 29, 1–6.

Hornby, B.E., Schwartz, L.M., Hudson, J.A., 1994. Anisotropic effective-medium modeling of the elastic properties of shales. Geophysics 59 (10), 1570–1583.

Hu, Q., Chen, X., Guo, Y., 2013. A rock physics model of kerogen inclusions in shale. SEG Technical Program Expanded Abstracts 2013.

Huang, K., Zhang, Z.N., Ghassemi, A., 2021. Virtual multi-dimensional internal bonds model with fracture energy conservation for three-dimensional numerical simulation of laboratory scale fluid pressurized fracturing. Int. J. Numer. Anal. Met. 45, 2214–2234.

Huo, B., Zhang, R., Zeng, Y., Fu, W., Muhadasi, Y., Chen, M., 2018a. Analysis of hydraulic fracture initiation and propagation in deep shale formation with high horizontal stress difference. J. Petrol. Sci. Eng. 170.

Huo, Z., Zhang, J., Li, P., Tang, X., Yang, X., Qiu, Q., Dong, Z., Li, Z., 2018b. An improved evaluation method for the brittleness index of shale and its application — A case study from the southern north China basin. J. Nat. Gas Sci. Eng. 59, 47–55.

Jia, Y., Tang, J., Lu, Y., Lu, Z., 2020. Laboratory geomechanical and petrophysical characterization of Longmaxi shale properties in Lower Silurian Formation, China. Mar. Petrol. Geol. 124, (8) 104800.

Kachanov, M., Tsukrov, I., Shafiro, B., 1994. Effective Elastic Properties of Solids with Randomly Located Defects. Springer, Netherlands, 269, 225-240.

Labani, M.M., Rezaee, R., 2015. The importance of geochemical parameters and shale composition on rock mechanical properties of gas shale reservoirs: a case study from the Kockatea Shale and Carynginia Formation from the Perth Basin, Western Australia. Rock Mech. Rock Eng. 48 (3), 1249–1257.

Li, Y., Chen, J., Yang, J.H., Liu, J., Tong, W., 2021. Determination of shale macroscale modulus based on microscale measurement: a case study concerning multiscale mechanical characteristics. Petrol. Sci., https://doi.org/10.1016/j.petsci.2021.10.004.

Li, Y., Yang, J., Pan, Z., Tong, W., 2020. Nanoscale pore structure and mechanical property analysis of coal: An insight combining AFM and SEM images. Fuel 260, 116352.

Li, Y., Wang, Z., Pan, Z., Niu, X., Yu, Y., Meng, S., 2019. Pore structure and its fractal dimensions of transitional shale: A cross section from east margin of the Ordos Basin, China. Fuel 241, 417–431.

Liang, K., Xie, L., He, B., Zhao, P., Hu, W., 2021. Effects of grain size distributions on the macro-mechanical behavior of rock salt using micro-based multiscale methods. Int. J. Rock Mech. Min. 138, (3–4) 104592.

Liu, D., Liu, H., Wu, Y., Zhang, W., Wang, Y., Santosh, M., 2022. Characterization of geo-material parameters: Gene concept and big data approach in geotechnical engineering. Geosyst. Geoenviron. 1, 100003.

Ly, T.H., Zhao, J., Cichocka, M.O., Li, L., Lee, Y.H., 2017. Dynamical observations on the crack tip zone and stress corrosion of two-dimensional MoS_2. Nat. Commun. 8, 14116.
Ma, Y., Pan, Z., Zhong, N., Connell, L.D., Down, D.I., Lin, W., Zhang, Y., 2016. Experimental study of anisotropic gas permeability and its relationship with fracture structure of Longmaxi Shales, Sichuan Basin, China. Fuel 180, 106–115.
Meier, T., Rybacki, E., Backers, T., Dresen, G., 2015. Influence of bedding angle on borehole stability: a laboratory investigation of transverse isotropic oil shale. Rock Mech. Rock Eng. 48 (4), 1535–1546.
Milliken, K.L., Hayman, N.W., 2019. Mudrock components and the genesis of bulk rock properties: review of current advances and challenges. Shale: Subsurface Science and Engineering. American Geophysical Union.
Moradian, Z., Einstein, H.H., Ballivy, G., 2016. Detection of fractureing levels in brittle rocks by parametric analysis of the acoustic emission signals. Rock Mech. Rock Eng. 49 (3), 785–800.
Neto, L.B., Kotousov, A., Bedrikovetsky, P., 2011. Application of contact theory to evaluation of elastic properties of low consolidated porous media. Int. J. Fracture 168 (2), 267–276.
Ougier-Simonin, A., Renard, F., Boehm, C., Vidal-Gilbert, S., 2016. Microfracturing and microporosity in shales. Earth-Sci Rev. 162, 198–226.
Panizza, G., Ravazzoli, C., 2019. An efficient rock-physics workflow for modeling and inversion in anisotropic organic-shales. J. Petrol. Sci. Eng. 180, 1101–1111.
Shahin, H.M., Nakai, T., Okuno, T., 2019. Numerical study on 3D effect and practical design in shield tunneling. Undergr. Space. 4, 201–209.
Shi, X., Jiang, S., Lu, S., He, Z., Li, D., Wang, Z., Xiao, D., 2019. Investigation of mechanical properties of bedded shale by nanoindentation tests: A case study on Lower Silurian Longmaxi Formation of Youyang area in southeast Chongqing, China. Petrol. Explor. Dev. 46 (1), 163–172.
Shimizu, H., Murata, S., Ishida, T., 2011. The distinct element analysis for hydraulic fracturing in hard rock considering fluid viscosity and particle size distribution. Int. J. Rock Mech. Min. 48 (5), 712–727.
Shrey, A., Brijes, M., 2015. Investigation of the failure mode of shale rocks in biaxial and triaxial compression tests. Int. J. Rock Mech. Min. 79, 109–123.
Simon, E., Moshe, E., Ruarri, J.D., Ronny, H., Calum, I.M., 2016. Impact of thermal maturation on nano-scale elastic properties of organic matter in shales. Mar Petrol Geol. 70, 175–184.
Sone, H., Zoback, M.D., 2013. Mechanical properties of shale-gas reservoir rocks — Part 1: Static and dynamic elastic properties and anisotropy. Geophysics 78 (5), D381–D392.
Sun, L., Liu, Q., Grasselli, G., Tang, X., 2020a. Simulation of thermal fracturing in anisotropic shale formations using the combined finite-discrete element method. Comput. Geotechnol. 117, 103237.
Sun, W., Zuo, Y., Wu, Z., Liu, H., Luo, X., 2020b. The distribution characteristics of brittle minerals in the Lower Cambrian Niutitang Formation in northern Guizhou. J. Nat. Gas Sci. Eng. 86, 103752.
Tobing, P.F.L., Feranie, S., Latief, F.D.E., 2016. Preliminary study of 2D fracture upscaling of geothermal rock using IFS fractal model. J. Phys. Conf. Ser. 739, (1) 012095.
Vernik, L., Nur, A., 1992. Petrophysical analysis of the Cajon Pass Scientific Well: Implications for fluid flow and seismic studies in the continental crust. J. Geophy.l Res. 97, 5121–5134.
Wang, B., Chen, Y., Lu, J., Jin, W., 2018. A rock physics modelling algorithm for simulating the elastic parameters of shale using well logging data. Sci. Rep. 8, 12151.
Wang, Y., Li, X., Wang, H., Dai, B., 2019. Developmental characteristics and geological significance of the bentonite in the Upper Ordovician Wufeng – Lower Silurian Longmaxi Formation in eastern Sichuan Basin, SW China. Petrol. Explor. Dev. 46 (4), 687–700.
Weijermars, R., Wang, J., Nelson, R., 2020. Stress concentrations and failure modes in horizontal wells accounting for elastic anisotropy of shale formations. Earth-Sci Rev. 200, 102957.
Wetherington, J.M., Steer, M.B., 2012. Standoff acoustic modulation of radio frequency signals in a log-periodic dipole array antenna. IEEE Antennas Wirel. Propag. Lett. 11, 885–888.
Wild, K., Amman, F., 2018. Experimental study of the hydro-mechanical response of Opalinus Clay – Part 1: Pore pressure response and effective geomechanical properties under consideration of confinement and anisotropy. Eng. Geol. 237, 32–41.
Wu, Y., Li, Y., Luo, S., Lu, M., Zhou, N., Wang, D., Zhang, G., 2020. Multiscale elastic anisotropy of a shale characterized by cross-scale big data nanoindentation. Int. J. Rock Mech. Min. 134, 104458.
Xu, X., Zeng, L., Tian, H., Ling, K., Che, S., Yu, X., Shu, Z., Dong, S., 2021. Controlling factors of lamellation fractures in marine shales: A case study of the Fuling Area in Eastern Sichuan Basin, China. J. Petrol. Sci. Eng. 12, 109091.
Yan, W., Yang, L., 2019. The effect of unit cell size and topology on tensile failure behavior of 2D lattice structures. Int. J. Mech. Sci. 170, 105342.
Zhang, X., Shi, W., Hu, Q., Zhang, S., Hu, H., Wang, X., Xu, Z., 2017. Geological controls and methane sorption capacity of marine shales of the Fuling shale gas field in the eastern Sichuan Basin, China. Pet. Geosci. 23 (4), 466–475.
Zhang, S.W., Shou, K.J., Xian, X.F., Zhou, J.P., Liu, G.J., 2018. Fractal characteristics and acoustic emission of anisotropic shale in Brazilian tests. Tunnel. Undergr. Space Technol. 71, 298–308.
Zhang, W.G., Zhang, R.H., Han, L., Goh, A., 2019. Engineering properties of Bukit Timah granitic residual soils in Singapore. Undergr. Space 4, 98–108.
Zhao, J., Zhang, D., 2020. Dynamic microscale fracture propagation in shale. Eng. Fract. Mech. 228, 106906.
Zhou, X.P., Zhao, Z., 2020. Digital evaluation of nanoscale-pore shale fractal dimension with microstructural insights into shale permeability. J. Nat. Gas Sci. Eng. 75, 103137.
Zou, C., Dong, D., Wang, Y., Li, X., Huang, J., Wang, S., Guan, Q., Zhang, C., Wang, H., Liu, H., 2016. Shale gas in China: characteristics, challenges and prospects (II). Petrol. Explor. Dev. 43 (2), 182–196.
Zou, C., Zhu, R., Chen, Z., James, G.O., Wu, S., Dong, D., Qin, Z., Wang, Y., Wang, L., Lin, S., Cui, J., Su, L., Cui, J., Su, L., Yang, Z., 2019. Organic-matter-rich shales of China. Earth-Sci. Rev. 189, 51–78.